Chemical Science

EDGE ARTICLE

View Article Online
View Journal | View Issue

Cite this: *Chem. Sci.*, 2020, **11**, 474

All publication charges for this article have been paid for by the Royal Society of Chemistry

In situ transfer of $CH_3NH_3PbI_3$ single crystals in mesoporous scaffolds for efficient perovskite solar cells†

Yanjun Guan,‡[a] Mi Xu,‡[a] Wenhao Zhang,[a] Da Li,[a] Xiaomeng Hou,[a] Li Hong,[a] Qifei Wang,[a] Zhihui Zhang,[a] Anyi Mei,[a] Min Chen,[b] Yuanyuan Zhou,[b] Nitin P. Padture,[b] Yue Hu,*[a] Yaoguang Rong*[a] and Hongwei Han[a]

Received 29th September 2019
Accepted 19th November 2019

DOI: 10.1039/c9sc04900b

rsc.li/chemical-science

Printable mesoscopic perovskite solar cells are usually fabricated by drop-casting perovskite precursor solution on a screen-printed mesoporous TiO_2/ZrO_2/carbon triple-layer followed by thermal annealing. They have attracted much attention due to their simple fabrication process and remarkable stability. However, challenges lie in how to achieve complete pore fillings of perovskites in the meso-pores and to obtain high-quality perovskite crystals. Here, we report an *in situ* crystal transfer (ICT) process based on gas–solid interaction to deposit perovskite $CH_3NH_3PbI_3$ absorber in the scaffold. $CH_3NH_3PbI_3$ single crystals are first transformed into a liquid phase *via* exposure to methylamine gas flow. After complete infiltration into the nano-structured scaffolds, the liquid phase is converted back to the solid phase with reduction of methylamine gas partial pressure, maintaining the high-quality of $CH_3NH_3PbI_3$ single crystals. Compared with the conventional drop-casting method, the ICT method effectively leads to interconnected morphology and prolongs the charge-carrier lifetime (from ~37.52 ns to ~110.85 ns) of the perovskite absorber in the scaffold. As a result, the devices can deliver a power conversion efficiency of 15.89%, which is attributed to the suppressed charge recombination and correspondingly enhanced open-circuit voltage of 0.98 V.

Introduction

The past decade has witnessed a rapid evolution of hybrid organic–inorganic perovskite solar cells (PSCs) as serious contenders to rival the leading photovoltaic technologies with both low cost and high power conversion efficiency (PCE).[1–3] The rapid growth of PCE is attributed to many research efforts on device architectures as well as processing techniques, but primarily to optimization of the quality of the perovskite thin films, *e.g.*, high crystallinity and few defects.[4–9] To achieve a uniform, high-crystallinity perovskite film, various processing techniques have been explored, such as sequential deposition,[8] anti-solvent method,[5] vacuum-assisted,[10] vapor-assisted[11] methods, *etc.* In parallel to the development of film processing techniques, various device architectures have also been studied. Among them, devices based on a TiO_2/ZrO_2/carbon triple mesoscopic architecture have attracted attention for the simple fabrication route and lower costs as a result of omitting the hole transport layer (HTL) and replacing the gold back-contact with carbon materials.[12] The mesoporous layers are prepared by screen-printing technique followed by sintering. Subsequently, the perovskite precursors are drop-casted into the scaffold. The organic–inorganic halide perovskite then crystallizes through solution *via* thermal annealing. Due to the difficulty in controlling the crystal growth in such thick layers with meso-pores, a large number of grain boundaries and point defects exist in the perovskite. These locations become recombination centers that inhibit further improvements of the device performance.[13] At the same time, large lattice mismatch and non-uniform contact between the perovskite and electron transport layer leads to the distortion of the crystal structure, which produces deep trap-states and reduces the output voltage. Unfortunately, most of the deposition methods that worked effectively in PSCs based on other structures do not work in this triple mesoscopic PSCs. In this structure, the priority is to achieve maximum pore filling of the mesoporous TiO_2 with high quality perovskite absorbers for enhanced light harvesting and charge-carrier separation and transport.

Previously, we have developed various strategies to improve the perovskite quality in the mesoporous scaffold, such as chemical engineering of the perovskite precursor solution by

[a]*Michael Grätzel Center for Mesoscopic Solar Cells, Wuhan National Laboratory for Optoelectronics, China-EU Institute for Clean and Renewable Energy, Huazhong University of Science and Technology, Wuhan 430074, Hubei, P. R. China. E-mail: ygrong@hust.edu.cn; yuehu@hust.edu.cn*

[b]*School of Engineering, Brown University, Providence, RI 02912, USA*

† Electronic supplementary information (ESI) available. See DOI: 10.1039/c9sc04900b

‡ These authors contributed equally to this work.

adding multi-functional additives,[14] tuning the crystallization process,[15] and employing post-treatments.[16] The perovskites with higher crystallinity and reduced trap density have enabled a PCE of over 15% for printable mesoscopic PSCs. In particular, the treatment of $MAPbI_3$-based ($MA^+ = CH_3NH_3^+$) cells with methylamine (MA^0) gas[16] results in the formation of a liquid intermediate $MAPbI_3 \cdot xMA^0$, which upon degassing yields perovskite reconstructed crystals with improved crystallinity and a high PCE of 15.2%. Zhou, *et al.* utilized the same method to improve the crystallinity of $MAPbI_3 \cdot MACl$ perovskite in order to reduce grain-boundary density.[17] Han, *et al.* used MA^0 gas to dissolve MAI and PbI_2 into a liquid-state mixture, followed by a soft-cover method for depositing perovskite films.[6] It has been proposed that the MA^0 gas treatment of $MAPbI_3$ induces rapid defect-healing of perovskite films at room temperature.[18–21] In this process the lone-pair electrons on N in the MA^0 molecule interact with the octahedral framework of PbI_6^{4-} in $MAPbI_3$. This causes the $MAPbI_3$ perovskite structure to collapse completely, and forms the liquid phase of $MAPbI_3 \cdot xMA^0$. It is also likely that this phase is a colloid rather than a pure liquid. Upon removal of the MA^0 gas, the MA^0 molecule is gradually released from the liquid phase, and the perovskite structure of $MAPbI_3$ is reconstructed.

Considering the phase transitions of $MAPbI_3$ with MA^0 gas, we attempted to directly transfer $MAPbI_3$ single crystals into the mesoporous TiO_2/ZrO_2/carbon scaffold of printable PSCs. $MAPbI_3$ single crystals possess low defect state density, for which the carrier diffusion length can reach 175 ± 25 μm, with a carrier mobility of 164 ± 25 cm^2 V^{-1} s^{-1}.[22,23] Inspired by the above work, we report here an *in situ* transfer process that transforms $MAPbI_3$ single crystals into a liquid phase *via* exposing them to MA^0 gas flow and fills in triple mesoscopic scaffolds. When the liquid phase completely infiltrates into the nano-structured scaffolds and subsequently converts back to solid-state phase, high-quality $MAPbI_3$ crystals form within the scaffold. Owing to the interconnected morphology, and preferred crystal orientation of ICT-process deposited $MAPbI_3$, the devices obtained have a maximum PCE of 15.89%. The perovskite film with low defect density resulted in suppressed charge recombination and correspondingly enhanced open-circuit voltage (V_{OC}). The ICT process is different from conventional solution processes. It does not involve liquid solvent or additional post-annealing processing, thus providing a promising prospect for PSCs application.

Results and discussion

$MAPbI_3$ single crystals were synthesized using procedures described in the literature.[24] Large-sized single crystals were grown from seed crystals in a supersaturated solution taking up to 2 days. The as-grown single crystals were ground into fine powders for the device fabrication, as illustrated schematically in Fig. 1a. To transfer the $MAPbI_3$ crystals into the mesoporous scaffolds, a homemade prototype reactor was designed, as shown in Fig. 1b and S1.† Briefly, the reactor was firstly pumped to −0.1 MPa pressure to remove the air, and then refilled with MA^0 gas with a low pressure of ~0.015 MPa which was found to be optimum for delivering the highest quality perovskite.[25] The whole process was performed at room temperature (RT) ~25 °C. Once the MA^0 gas was refilled into the reactor, the $MAPbI_3$ crystal powders began to turn into the liquid phase $MAPbI_3 \cdot xMA^0$. As shown in Reaction 1, CH_3NH_2 gas (g) reacts with the inorganic PbI_6-octahedra framework in $MAPbI_3$ perovskite crystals (s) resulting in the collapse of the perovskite structure into the liquid state (l). Within ~3 minutes of MA^0 gas exposure, the mixture of $MAPbI_3$ crystals and liquid-state phase $MAPbI_3 \cdot xMA^0$ completely converted into transparent colloidal liquid-state phase $MAPbI_3 \cdot xMA^0$, spreading and penetrating in the mesoporous scaffolds. The treating time refers to the time

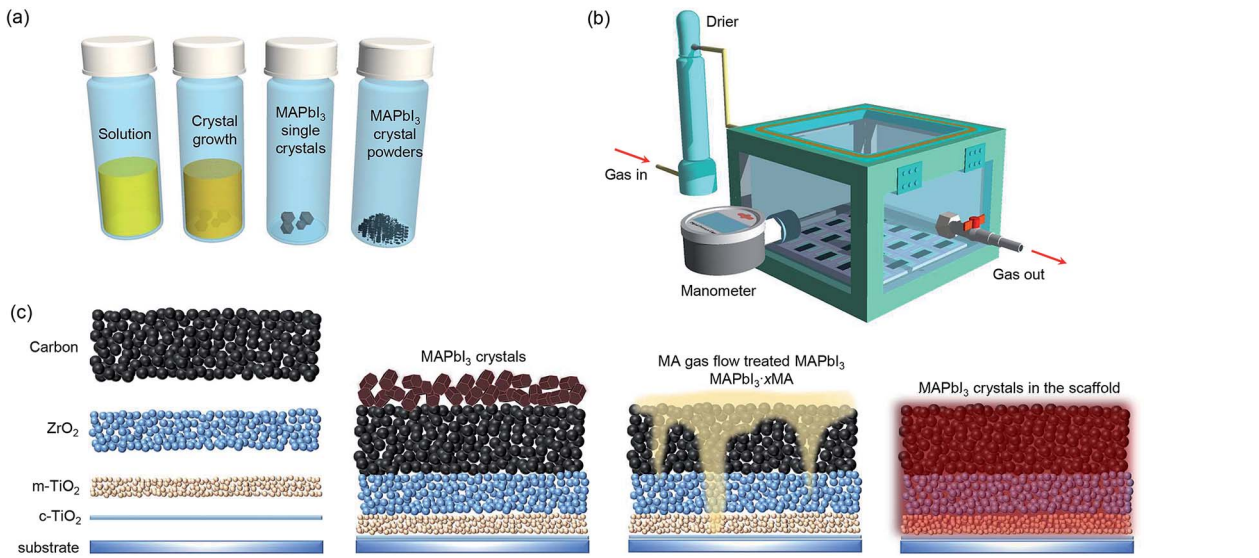

Fig. 1 Schematic illustration of the: (a) $MAPbI_3$ single crystals and powders preparation process, (b) ICT reactor (the digital images are shown in Fig. S1†), and (c) ICT process from blank scaffold to perovskites infiltrated scaffold.

which transparent colloidal liquid-state phase spreads and penetrates in the mesoporous scaffolds by capillary action or gravity. After full penetration (~35 minutes) of the colloidal liquid-state phase, the reactor was refilled with N_2 flow for over 30 minutes. Upon reduction of MA^0 gas partial pressure, the liquid phase slowly transformed back to dark brown $MAPbI_3$, forming high-quality perovskite absorber within the scaffold (confirmed by XRD measurements), as per Reaction 2. More detailed description of the ICT process is included in the experimental section of the (ESI†). Above all, the experimental procedure is easy to perform, as shown schematically in Fig. 1c.

$$CH_3NH_3PbI_3(s) + xCH_3NH_2(g) \rightarrow CH_3NH_3PbI_3 \cdot xCH_3NH_2(l) \quad (1)$$

$$CH_3NH_3PbI_3 \cdot xCH_3NH_2(l) \rightarrow CH_3NH_3PbI_3(s) + xCH_3NH_2(g) \quad (2)$$

The mesopore filling situation and morphology of the perovskite absorber in the scaffold were characterized by scanning electron microscopy (SEM). As shown in Fig. 2a and b, the drop-casting method resulted in incomplete pore fillings of the perovskite absorber in the mesoporous scaffold due to the fast and uncontrolled crystallization of the perovskite precursors.[26] For the ICT process, the perovskite absorber completely filled up the mesopores and formed a compact morphology, as shown in Fig. 2c–f. By prolonging the treating time from ~9 min (Fig. 2d) to ~35 min (Fig. 2f), the morphology of the perovskites turned more compact. The top-view SEM images of $MAPbI_3$ films deposited on mesoporous TiO_2 by the two methods were shown in Fig. S2.† The drop-casting method resulted in a rough surface with needle-shaped crystals and holes/voids on the $MAPbI_3$ film. In contrast, the perovskite film prepared by the ICT method demonstrates full coverage on the substrate. The distributions of the perovskite absorber in the mesoporous scaffold were further characterized by energy dispersive spectroscopy (EDS) measurements, confirming that all elements are distributed uniformly (Fig. S3†). In addition, less gaps between the perovskite domains and with mesoporous TiO_2 layer will lead to less interface combination, which will undoubtedly make contributions to the voltage of the device. Here it should be emphasized that the after transferring to the scaffold, the perovskite single crystals turned into well-connected polycrystalline perovskite networks instead of forming another perovskite single crystal.

Owing to the improved mesopore filling and compact morphology of the ICT-deposited perovskite absorber in the mesoporous TiO_2 scaffold, the absorption was also significantly enhanced, as shown in Fig. 3a. For the crystallinity of the perovskite absorber, the (110) and (220) peak intensities of $MAPbI_3$ deposited using the ICT method are much higher than those obtained using the drop-casting method, as shown in Fig. 3b. Besides, the clear spilt of the (220) and (004) peaks also indicates that the ICT-deposited perovskite adopts a tetragonal phase with higher crystalline quality.[24] Furthermore, 2D X-ray diffraction (2D-XRD) images were obtained for directly revealing the texture of the thin films. As seen in Fig. 3c, the

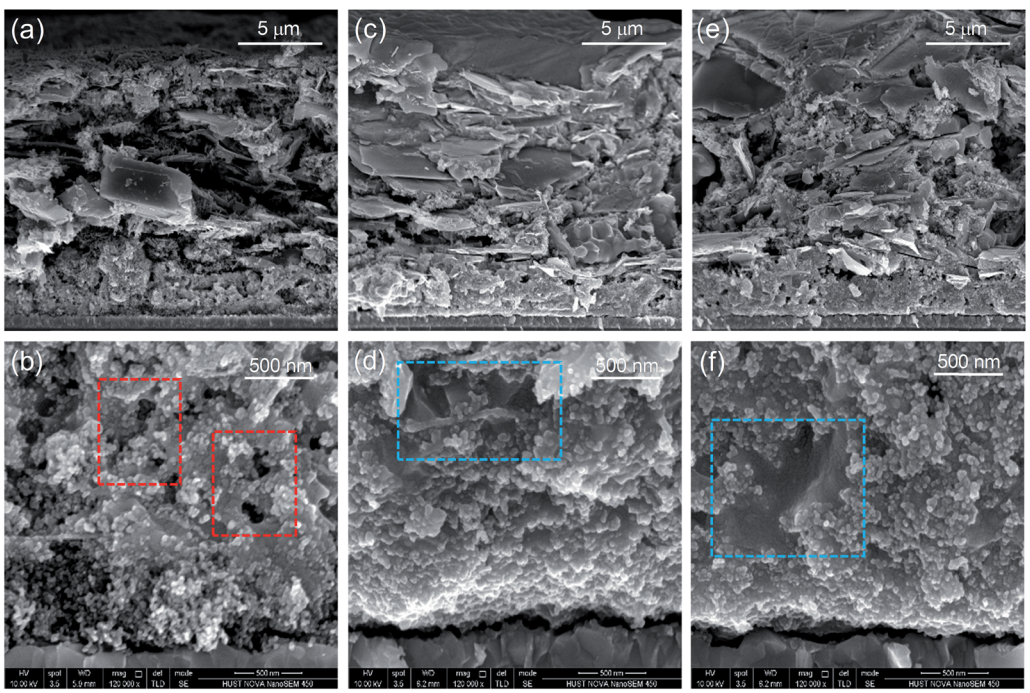

Fig. 2 The cross-sectional SEM images of the device fabricated with (a and b) the drop-casting method and (c–f) the ICT method. Devices in (c and d) were treated for ~9 minutes, and devices in (e and f) were treated for ~35 minutes. The regions of the mesoporous scaffold that have not been filled by the perovskite absorber are marked by red rectangles. The connection between the perovskite absorber in the mesopores can be enhanced by prolonging the treating time, as in regions marked by blue rectangles.

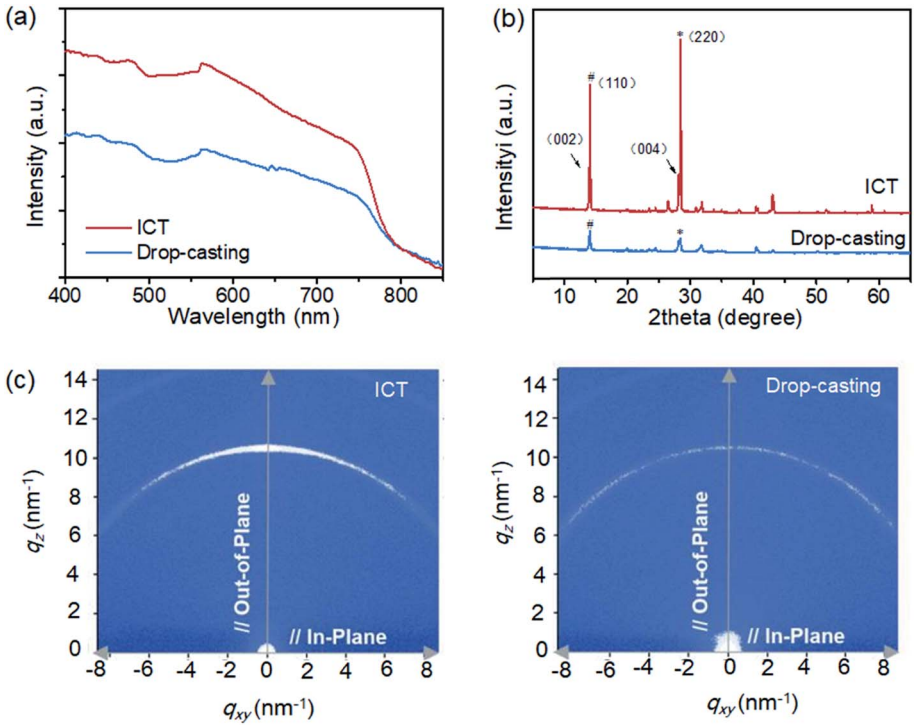

Fig. 3 Comparison of (a) UV-vis absorption spectra and (b) XRD spectra of $MAPbI_3$ films deposited on mesoporous TiO_2 scaffold using the drop-casting method and the ICT method. (c) 2D-XRD images of $MAPbI_3$ films on mesoporous ZrO_2 scaffold using the drop-casting method (right) and the ICT method (left).

(110) reflection of the perovskite film made using the drop-casting method showed a uniform spread along the Debye–Scherrer ring, indicative of random orientations of the grains. However, with the introduction of the ICT method, the Debye–Scherrer ring becomes discrete and a strong (110) texture is observed.[27,28] The more anisotropic nature of the perovskite film *via* the ICT process may contribute positively to the charge-carrier dynamics discussed later.

The carrier photoluminescence (PL) behaviour of $MAPbI_3$ perovskite prepared by spin-coating and ICT methods on ZrO_2 scaffolds were studied using the ISS Q2 laser scanning microscope in conjunction with FastFLIM, which is a digital frequency domain technique that can simulate both the PL intensity and lifetime of a sample simultaneously. Since a perovskite capping layer usually emerges on top of the mesoporous scaffold, the nature of the perovskite on the surface and within the mesopores is expected to different. However, the high resolution of the laser scanning microscope allows one to separate the perovskite on the surface and that in the mesopores by tuning the focus location. As shown in Fig. 4a, the perovskite tends to crystallize into separate islands in the spin-coating method. Randomly located dark regions with zero intensity exist both on the surface and within the mesopores. These inhomogeneous dark regions indicate extremely low content of perovskite, indicating voids or incomplete pore-fillings. In contrast, the sample prepared by ICT method shows PL with increased intensity (Fig. 4b). These perovskite regions are larger and brighter. The lifetime images are produced by bi-exponential fitting of each pixel and then taking the intensity-weighted average lifetime of the two components. Besides, the lifetime histograms are plotted to compare the difference of lifetime distributions. As shown in Fig. 4c, the average PL lifetime is much enhanced in the films deposited using the ICT method compared with those using spin-coating method. In the ICT method, the crystals tend to grow larger on the surface than in the pores, giving an average PL lifetime of ~131.29 ns on the surface and ~110.85 ns in the mesopores. In contrast, for the films prepared using the spin-coating method, the average PL lifetime on the surface is ~33.80 ns and ~37.52 ns within the mesopores. The longer lifetime indicates a lower trap state density when ICT method is used to deposit the $MAPbI_3$ film. Conventional PL measurements (Horiba HR800s) were also conducted, as shown in Fig. S4.† The central excitation peak position of the two methods in steady-state PL spectra is blue-shifted from 772 nm for the drop-casting method to 762 nm for the ICT method. This is because the shallow-level defects in the film prepared by the ICT method are reduced, and thus obtain a perovskite layer with high quality.[29,30] This is also consistent with the improvement in crystallinity from XRD results.

The photovoltaic performance parameters are illustrated in Table 1 in consistent with the cross-sectional SEM results above. The devices prepared by the drop-casting method achieve an average efficiency of 7.95% and a voltage of only 0.87 V. Whereas, using the ICT method, with a MA-gas-treatment duration of ~9 minutes, PCE up to 9.45% is obtained. The

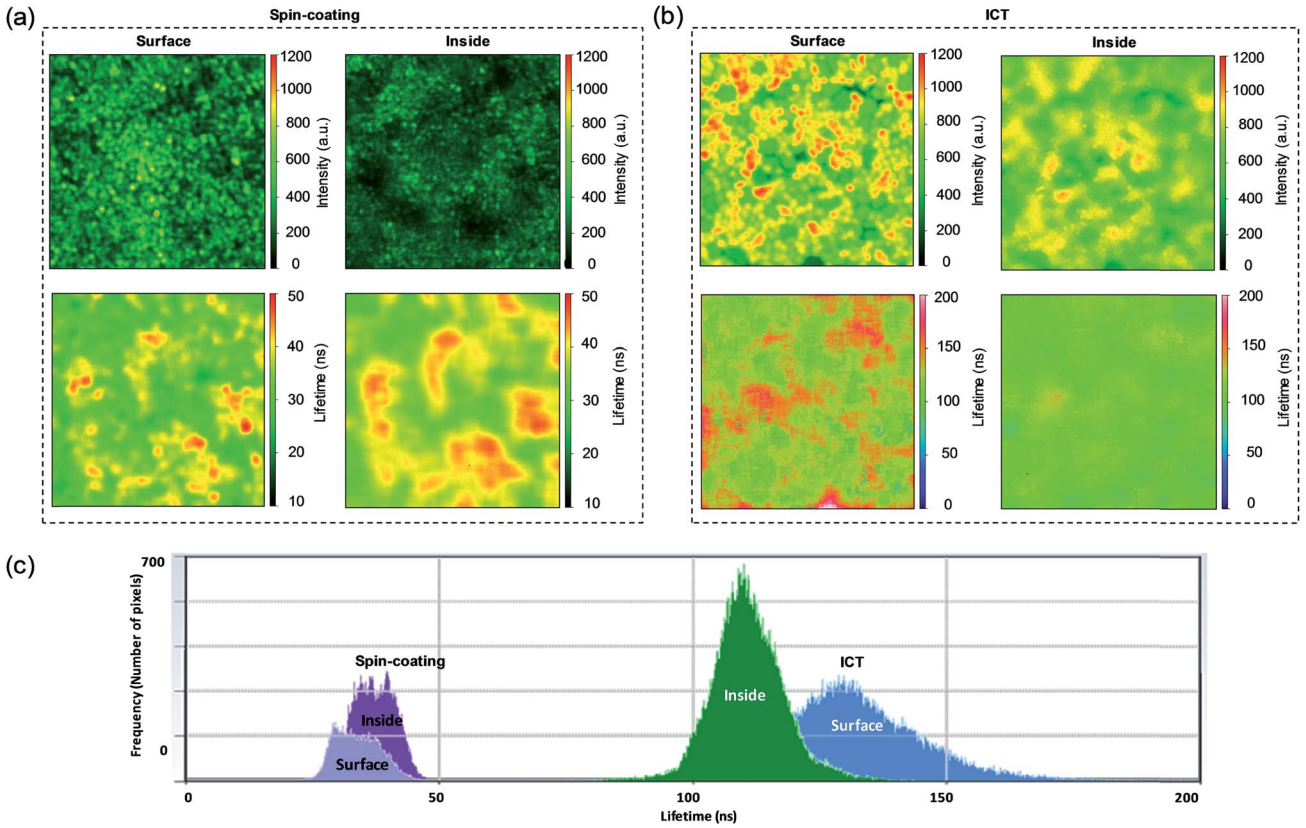

Fig. 4 The photoluminescence and lifetime imaging results for (a) spin-coated $MAPbI_3$ and (b) ICT-deposited $MAPbI_3$ on mesoporous ZrO_2 scaffold (data collected both on surface and inside are shown). (c) The lifetime histograms of each sample are shown both on surface and inside (note: in order to avoid the formation of a capping layer on the mesoporous scaffold, spin-coating method was used instead of drop-casting method in this experiment).

Table 1 Comparison of *J–V* parameters of devices fabricated using the two different methods

	V_{OC} (V)	J_{SC} (mA cm^{-2})	FF	PCE (%)
Drop-casting	0.87 ± 0.03	16.75 ± 0.36	0.55 ± 0.08	7.95 ± 1.20
ICT (~9 min)	0.88 ± 0.02	19.19 ± 2.84	0.56 ± 0.09	9.45 ± 1.18
ICT (~30 min)	0.96 ± 0.04	22.18 ± 0.71	0.65 ± 0.08	13.83 ± 1.34

short-circuit current density (J_{SC}) is effectively improved because of the low density of gross defects such as voids in the mesoporous film. In addition, the quality of the perovskite film using the ICT method is also significantly higher than that using the drop-casting method. When the MA^0 gas treatment time is ~35 minutes, the perovskite film becomes continuous and dense (Fig. 2e and f), increasing the average J_{SC} to 22.69 mA cm^{-2}. It is worth mentioning that due to better crystal quality, the carrier recombination in the device is reduced, and the average V_{OC} of the device is increased to 0.96 V.

In particular, we compared representative *J–V* curves of the champion cells fabricated using three methods in Fig. 5a. The simple one-step drop-casting method can only obtain a PCE of 9.09%. According to our results for the pure $MAPbI_3$ as the light absorber in triple-mesoscopic PSCs, the efficiency can be improved to over 13% by using a sequential deposition method or optimizing the solvents.[26,31] Previously, we have developed a MA^0 gas post-treatment method to enhance the performance of $MAPbI_3$ based cells.[20] The MA^0 gas can make the morphology of the perovskite more uniform and compact. Correspondingly, an average efficiency of over 14% was achieved (champion efficiency of 15.26%). Notably, this post-treatment method can only improve the morphology of the perovskite in the scaffold, but not enhancing the mesopore filling ratio. In addition, it might be difficult for MA^0 gas to reach the bottom of the scaffold and interact with the perovskite absorber there. For the ICT method, the perovskite crystals are able to adequately interact with MA^0 gas, then liquify and infiltrates in the scaffold. Correspondingly, an efficiency of 15.89% was achieved with an impressively high V_{OC} of 0.98 V, an enhanced J_{SC} of 22.98 mA cm^{-2}, and FF of 0.71. The distribution of the V_{OC}, J_{SC}, FF and PCEs for 15 devices is illustrated in Fig. 5b. Compared with drop-casting method, ICT method showed better reproducibility, especially in terms of V_{OC} and J_{SC}, and achieved a V_{OC} of up to 0.98 V. The incident photon-to-current conversion efficiency (IPCE) spectra of the devices are illustrated in Fig. S5.† It is confirmed that the increased J_{SC} is due to the enhanced light harvesting ability from 400 nm to 800 nm. Furthermore, the higher IPCE between 500 nm and 800 nm can be also related to the suppressed recombination reactions.

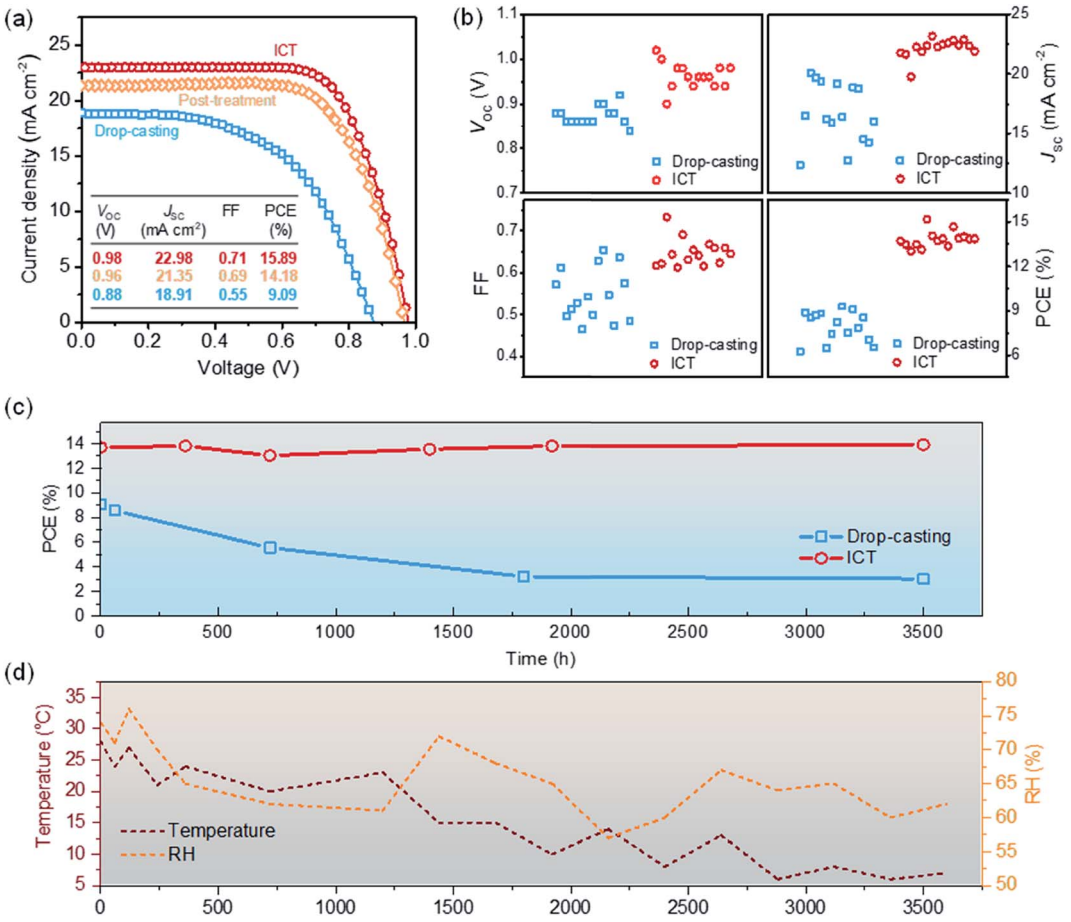

Fig. 5 Comparison of (a) J–V curves and (b) distributions of the V_{OC}, J_{SC}, FF, and PCE for 15 printable mesoscopic PSCs in reverse scan. (c) PCEs of PSCs as a function exposure to the ambient atmosphere for up to 3500 hours. (d) The ambient temperature and relative humidity during the storage.

In order to explore the underlying mechanisms responsible for the excellent performance of the device, electrochemical impedance spectroscopy of devices under the bias of 0 to −0.8 V in dark was tested. Fig. S6† shows the Nyquist plots of devices made using the two different methods at a bias of −0.5 V. The inset is the circuit employed to fit the plots. There is only one arc in the figure[32] which represents the charge transfer resistance (R_{CT}) of the whole device. With the increase of the applied bias voltage, R_{CT} of the device fabricated using the ICT method drops slowly. On the one hand, the density of defects in the perovskite layer is expected to be lower because of the enhanced crystallinity in the device prepared using the ICT method. On the other hand, the perovskite single crystals fill up the mesoporous structure assisted by the MA^0 gas with improved interface contact between the carbon electrode and the mesoporous TiO_2 layer, thus the carrier accumulation and recombination at the interface is expected to be lower. This may provide an explanation of the high V_{OC} in devices fabricated using the ICT method.

Notably, Hinsch, *et al.* has reported a similar molten-salt approach for depositing perovskite absorbers in the mesoporous scaffold.[33] $MAPbI_3$ powders were used as the perovskite source and acetonitrile (ACN) was used to tune the viscosity of the precursor. A high voltage of 1 V was obtained, although the overall PCE was only 12.6%. This work also emphasized the key concept of our method. We employed $MAPbI_3$ single crystals as the perovskite sources instead of normal perovskite powders. It is believed that the enhanced performance is due to the high quality of the perovskite crystals, and the ICT process can maintain the excellent properties after transferring them into the mesoporous scaffold.[34]

Besides the efficiency, the stability of the cells fabricated with ICT method was also improved. The cells were fabricated in ambient air and continuously monitored in laboratory environment without encapsulations for up to 3500 hours (Fig. 5c). The temperature was within the range of 4–35 °C, and the relative humidity (RH) was between 55% and 75%. The PCE of the device prepared using the drop-casting method decreased from the initial 9.09% to 5.89% after 1000 h. After 3500 h, the PCE of the device dropped to 3%. Under the same conditions, the efficiency of the cells prepared using ICT method was stable. Previously, we have investigated the ambient stability of triple mesoscopic PSCs based on $MAPbI_3$ under different RH.[15] The high RH may lead to the decomposition of the perovskite

absorber and causes severe performance degradation. Here for the cells fabricated by ICT method, the performance is relative insensitivity to the environment even with RH of over 70%. It is proposed that such enhanced ambient stability is due to the high crystallinity and compact morphology of perovskite absorber in the mesoporous scaffold. For further practical applications, the stability under continuous illumination or high temperature may be more important, although the high ambient stability benefits the mass-production of this PV technology. Unfortunately, for pure $MAPbI_3$, the inevitable release of I_2 may make it challenging to fabricate long-term stable PSCs.[35] Employing mixed-cations perovskites or interface modifications seems a promising route to achieve long-term stability.[36–38] Here for the ICT method, it can only transfer pure phase perovskites in the mesoporous scaffold at present. If other cations can be properly incorporated, or the interface can be tuned, higher stability under more harsh conditions may be expected.

Conclusions

We have demonstrated the use of the ICT method based on gas–solid interaction to deposit $MAPbI_3$ within mesoporous scaffolds. In this process, $MAPbI_3$ single crystals placed on top of the scaffolds are first transformed into a liquid phase *via* exposing them to MA^0 gas flow. After complete infiltration into the scaffolds, the liquid phase is converted back to solid phase, forming high-quality $MAPbI_3$ crystals with minimum volume shrinkage within the scaffold. As a result, the PSCs fabricated using the ICT method showed a PCE approaching 16%, which is attributed to the suppressed charge recombination and the correspondingly enhanced V_{OC}. We believe it is a promising technique for future upscaling manufacturing high quality perovskite thin films and related optoelectronics devices.

Conflicts of interest

There are no conflicts to declare.

Acknowledgements

The authors acknowledge financial support from the National Natural Science Foundation of China (Grant No. 21702069 and 91733301), the Fundamental Research Funds for the Central Universities, the Science and Technology Department of Hubei Province (No. 2017AAA190), the 111 Project (No. B07038), the Program for HUST Academic Frontier Youth Team (2016QYTD06), and the Double First-Class Research funding of China-EU Institute for Clean and Renewable Energy (No. ICARE-RP-2018-SOLAR-001 and ICARE-RP-2018-SOLAR-002). We thank the Analytical and Testing Center of Huazhong University of Science and Technology (HUST) for performing various characterization and measurements. M. C., Y. Z., and N. P. P. acknowledge the funding from the National Science Foundation (Grants OIA-1538893) and the Office Naval Research (Grant N00014-17-1-2232). The authors would also thank Dr Yan Guan and Dr Yuansheng Sun for performing the PL measurements.

References

1 Y. Rong, Y. Hu, A. Mei, H. Tan, M. I. Saidaminov, S. I. Seok, M. D. McGehee, E. H. Sargent and H. Han, *Science*, 2018, **361**, eaata8235.
2 J.-P. Correa-Baena, M. Saliba, T. Buonassisi, M. Grätzel, A. Abate, W. Tress and A. Hagfeldt, *Science*, 2017, **358**, 739.
3 Q. Jiang, Y. Zhao, X. Zhang, X. Yang, Y. Chen, Z. Chu, Q. Ye, X. Li, Z. Yin and J. You, *Nat. Photonics*, 2019, **13**, 460–466.
4 W. Tress, N. Marinova, T. Moehl, S. M. Zakeeruddin, M. K. Nazeeruddin and M. Gratzel, *Energy Environ. Sci.*, 2015, **8**, 995–1004.
5 N. J. Jeon, J. H. Noh, Y. C. Kim, W. S. Yang, S. Ryu and S. I. Seok, *Nat. Mater.*, 2014, **13**, 897–903.
6 H. Chen, F. Ye, W. Tang, J. He, M. Yin, Y. Wang, F. Xie, E. Bi, X. Yang, M. Grätzel and L. Han, *Nature*, 2017, **550**, 92–95.
7 X. Li, D. Bi, C. Yi, J.-D. Décoppet, J. Luo, S. M. Zakeeruddin, A. Hagfeldt and M. Grätzel, *Science*, 2016, **353**, 58–62.
8 J. Burschka, N. Pellet, S.-J. Moon, R. Humphry-Baker, P. Gao, M. K. Nazeeruddin and M. Grätzel, *Nature*, 2013, **499**, 316–319.
9 Y. Zhou, O. S. Game, S. Pang and N. P. Padture, *J. Phys. Chem. Lett.*, 2015, **6**, 4827–4839.
10 X. Zhang, G. Zhou, P. Shi, H. Du, T. Lin, J. Teng and F. S. Chau, *Opt. Lett.*, 2016, **41**, 1197–1200.
11 M. Liu, M. B. Johnston and H. J. Snaith, *Nature*, 2013, **501**, 395–398.
12 A. Mei, X. Li, L. Liu, Z. Ku, T. Liu, Y. Rong, M. Xu, M. Hu, J. Chen, Y. Yang, M. Grätzel and H. Han, *Science*, 2014, **345**, 295–298.
13 Y. Rong, L. Liu, A. Mei, X. Li and H. Han, *Adv. Energy Mater.*, 2015, **5**, 1501066.
14 Y. Hu, Z. Zhang, A. Mei, Y. Jiang, X. Hou, Q. Wang, K. Du, Y. Rong, Y. Zhou, G. Xu and H. Han, *Adv. Mater.*, 2018, **30**, 1705786.
15 Y. Rong, X. Hou, Y. Hu, A. Mei, L. Liu, P. Wang and H. Han, *Nat. Commun.*, 2017, **8**, 14555.
16 L. Hong, Y. Hu, A. Mei, Y. Sheng, P. Jiang, C. Tian, Y. Rong and H. Han, *Adv. Funct. Mater.*, 2017, **27**, 1703060.
17 F. Ji, S. Pang, L. Zhang, Y. Zong, G. Cui, N. P. Padture and Y. Zhou, *ACS Energy Lett.*, 2017, **2**, 2727–2733.
18 Z. Zhou, Z. Wang, Y. Zhou, S. Pang, D. Wang, H. Xu, Z. Liu, N. P. Padture and G. Cui, *Angew. Chem., Int. Ed.*, 2015, **54**, 9705–9709.
19 S. R. Raga, Y. Jiang, L. K. Ono and Y. Qi, *Energy Technol.*, 2017, **5**, 1750–1761.
20 Q. Wang, W. Zhang, Z. Zhang, S. Liu, J. Wu, Y. Guan, A. Mei, Y. Rong, Y. Hu and H. Han, *Adv. Energy Mater.*, 2019, DOI: 10.1002/aenm.201903092.
21 Y. Zhou and N. P. Padture, *ACS Energy Lett.*, 2017, **2**, 2166–2176.
22 Q. Dong, Y. Fang, Y. Shao, P. Mulligan, J. Qiu, L. Cao and J. Huang, *Science*, 2015, **347**, 967–970.
23 Z. Chen, Q. Dong, Y. Liu, C. Bao, Y. Fang, Y. Lin, S. Tang, Q. Wang, X. Xiao, Y. Bai, Y. Deng and J. Huang, *Nat. Commun.*, 2017, **8**, 1890.

24 Y. Liu, Z. Yang, D. Cui, X. Ren, J. Sun, X. Liu, J. Zhang, Q. Wei, H. Fan, F. Yu, X. Zhang, C. Zhao and S. Liu, *Adv. Mater.*, 2015, **27**, 5176–5183.
25 M. Long, T. Zhang, H. Zhu, G. Li, F. Wang, W. Guo, Y. Chai, W. Chen, Q. Li, K. S. Wong, J. Xu and K. Yan, *Nano Energy*, 2017, **33**, 485–496.
26 J. Chen, Y. Xiong, Y. Rong, A. Mei, Y. Sheng, P. Jiang, Y. Hu, X. Li and H. Han, *Nano Energy*, 2016, **27**, 130–137.
27 Z. Wang, Q. Lin, F. P. Chmiel, N. Sakai, L. M. Herz and H. J. Snaith, *Nat. Energy*, 2017, **2**, 17135.
28 Y. Zong, Y. Zhou, M. Ju, H. F. Garces, A. R. Krause, F. Ji, G. Cui, X. C. Zeng, N. P. Padture and S. Pang, *Angew. Chem., Int. Ed.*, 2016, **55**, 14723–14727.
29 D. W. de Quilettes, S. M. Vorpahl, S. D. Stranks, H. Nagaoka, G. E. Eperon, M. E. Ziffer, H. J. Snaith and D. S. Ginger, *Science*, 2015, **348**, 683–686.
30 Y. Shao, Z. Xiao, C. Bi, Y. Yuan and J. Huang, *Nat. Commun.*, 2014, **5**, 5784.
31 T. Liu, L. Liu, M. Hu, Y. Yang, L. Zhang, A. Mei and H. Han, *J. Power Sources*, 2015, **293**, 533–538.
32 H. Chen, Z. Wei, H. He, X. Zheng, K. S. Wong and S. Yang, *Adv. Energy Mater.*, 2016, **6**, 1502087.
33 L. Wagner, S. Chacko, G. Mathiazhagan, S. Mastroianni and A. Hinsch, *ACS Energy Lett.*, 2018, **3**, 1122–1127.
34 D.-N. Jeong, D.-K. Lee, S. Seo, S. Y. Lim, Y. Zhang, H. Shin, H. Cheong and N.-G. Park, *ACS Energy Lett.*, 2019, **4**, 1189–1195.
35 S. Wang, Y. Jiang, E. J. Juarez-Perez, L. K. Ono and Y. Qi, *Nat. Energy*, 2016, **2**, 16195.
36 M. Saliba, T. Matsui, K. Domanski, J.-Y. Seo, A. Ummadisingu, S. M. Zakeeruddin, J.-P. Correa-Baena, W. R. Tress, A. Abate, A. Hagfeldt and M. Grätzel, *Science*, 2016, **354**, 206–209.
37 G. Grancini, C. Roldán-Carmona, I. Zimmermann, E. Mosconi, X. Lee, D. Martineau, S. Narbey, F. Oswald, F. De Angelis, M. Graetzel and M. K. Nazeeruddin, *Nat. Commun.*, 2017, **8**, 15684.
38 N. Arora, M. I. Dar, A. Hinderhofer, N. Pellet, F. Schreiber, S. M. Zakeeruddin and M. Grätzel, *Science*, 2017, **358**, 768–771.